RECONSTRUCTION OF THE TIME-AVERAGED KEYHOLE GEOMETRY IN LASER BEAM WELDING ASSISTED WITH ELECTROMAGNETIC EFFECT

F. YANG*,**, X. MENG*, S. N. PUTRA*, M. BACHMANN*, M. RETHMEIER****,*,***

**Bundesanstalt für Materialforschung und -prüfung, 12205 Berlin, Germany*
***Production Technology Group, Technische Universität Ilmenau, 98693 Ilmenau, Germany*
****Fraunhofer – Institut für Produktionsanlagen und Konstruktionstechnik, 10587 Berlin, Germany*
*****Institut für Werkzeugmaschinen und Fabrikbetrieb, Technische Universität Berlin, 10587 Berlin, Germany*

DOI 10.3217/978-3-99161-089-2-008, license CC BY 4.0

ABSTRACT

In laser beam welding (LBW), the time-averaged keyhole shape provides statistical insights into the process compared to its transient geometry, offering a deeper understanding of the overall keyhole behaviour. However, capturing the time-averaged keyhole shape through experimental methods remains challenging. In this paper, a reconstruction algorithm for the time-averaged keyhole is developed and integrated into a three-dimensional transient multi-physical coupled numerical model. The algorithm can accurately capture the key characteristics of the keyhole, including its diameter and centroid. In addition, it can also successfully reproduce the experimentally observed phenomena of keyhole tailing. The overall shape of the keyhole appears smooth, without exhibiting obvious instability features. Furthermore, the time-averaged keyhole shape is compared under different magnetic flux densities when an external oscillating magnetic field is applied. The results indicate that the application of external magnetic fields does not fundamentally alter the overall keyhole shape. With increasing magnetic flux density, the trailing tail becomes progressively less pronounced and a noticeable increase in the curvature of the rear wall is observed. The spatial-average of standard deviation of the keyhole diameter can serve as an effective index for evaluating the keyhole instability. Keyhole stability in LBW of aluminium alloys is improved under the assistance of electromagnetic fields, and this stabilization is positively correlated with increasing magnetic flux density.

Keywords: laser beam welding; keyhole reconstruction; magnetic fields; porosity defects; keyhole stability.

INTRODUCTION

Deep penetration laser beam welding (LBW) is a high efficiency joining technique characterized by the formation of a keyhole, which is a cavity created by the recoil pressure generated during high power density laser irradiation. This keyhole enables deep penetration with a high aspect ratio, making LBW widely used in industries such as automotive manufacturing, shipbuilding, and aerospace [1-6]. However, the keyhole is inherently unstable due to complex interactions among laser energy absorption, vaporization induced recoil pressure, surface tension, and melt flow [7]. These instabilities manifest as geometric fluctuations in space and time, contributing significantly to the formation of common welding defects such as spatter, porosity, and spiking [8-10]. These defects can severely influence the mechanical performance of welded joints.

The assessment of keyhole instability remains challenging, owing to the inherently transient and nonlinear nature of the process, as well as the opacity of metals. Various approaches, including high-speed imaging [11], optical coherence tomography [12], and in-situ synchrotron X-ray imaging [9,13], have been employed to evaluate keyhole behaviour. However, these methods offer limited insights or require high costs, with restricted accessibility. Metal/glass configurations have been used for visualizing keyhole morphology [14], but the accuracy is limited because of the difference in thermal and optical properties between glass and metal.

Numerical simulations offer a valuable alternative for investigating keyhole dynamics with enhanced temporal and spatial resolution. Previous studies have used simulation-based metrics such as the keyhole depth fluctuation and the keyhole collapse frequency to assess its stability [15,16]. In addition, given that keyhole behaviour is mainly characterized by the changes in keyhole morphology, understanding the evolution of the keyhole shape is essential. Although experimental studies have explored transient and time-averaged keyhole morphologies by stacking thousands of frames [17], numerical simulations provide a lower cost alternative for capturing transient keyhole dynamics. Moreover, the investigations of time-averaged keyhole morphology based on numerical simulations are rare.

Recently, active control of keyhole behaviour has attracted increasing interest. While welding parameter adjustments and ambient pressure variations offer indirect control over keyhole dynamics [15,18], external magnetic fields provide a more direct method. External Lorentz forces can directly act on both the keyhole wall and the weld pool, affecting their behaviour [19].

In this study, we introduce an alternating magnetic field during laser beam welding to actively control the dynamic behaviour of the keyhole and weld pool via Lorentz force interaction. A novel keyhole reconstruction algorithm is developed to evaluate time-averaged keyhole morphologies under different magnetic field conditions. Based on this, a new stability assessment metric is proposed, enabling a systematic and quantitative analysis of keyhole stability. This work provides deeper insights into the mechanisms governing keyhole dynamics and offers a promising approach for improving weld quality in deep penetration laser beam welding.

EXPERIMENTAL PROCEDURE

LBW experiments were conducted using AlMg3 aluminium alloy plates with dimensions of 300 mm × 100 mm × 10 mm in bead-on-plate welding configuration. The laser source was an IPG YLR-20000 fibre laser, operating at a wavelength of 1070 nm with a focal beam diameter of 520 µm. The focus position was set at the top surface of the workpiece. The laser beam inclination was 10° with a forward angle relative to the vertical axis. A constant laser power of 6 kW and a welding speed of 2 m/min were used for all welding experiments. Argon shielding gas was supplied at a flow rate of 20 l/min to prevent oxidation of the weld pool.

To investigate the influence of electromagnetic forces on keyhole dynamics, oscillating magnetic fields were applied with a pole cross-section of 20 mm × 20 mm and a pole distance of 15 mm. The magnet poles were positioned 2 mm above the top surface of the base metal, as illustrated in Fig. 1. Oscillating magnetic fields were applied at a frequency of 2300 Hz, with root-mean-square (RMS) magnetic flux densities of 100 - 280 mT.

The internal weld quality in terms of porosity was quantified via X-ray inspection. Weld cross-sections were prepared by mechanical sectioning perpendicular to the welding direction and etched to reveal the fusion line. These etched profiles were used to validate the simulation results.

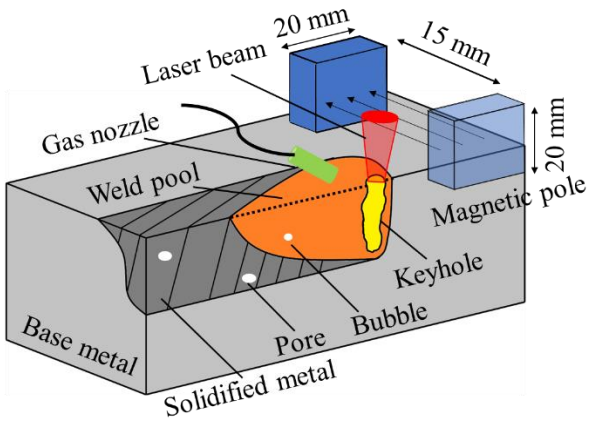

Fig. 1 Setup of the Laser Beam Welding experiments

MATHEMATICAL MODELING

To manage the complexity and nonlinearity of the laser beam welding process, several assumptions and simplifications were introduced to improve the solvability and computational efficiency of the mathematical model. The weld pool fluid was modelled as an incompressible, Newtonian, and laminar flow, with buoyancy effects included via the Boussinesq approximation. Seebeck effects, including thermoelectric currents and Joule heating, were

excluded. The magnetic flux density was assumed to remain unchanged along the transverse direction based on cold-condition measurements, with the aluminium alloy treated as having a relative magnetic permeability of one. Additionally, the keyhole gas phase was considered electrically non-conductive with uniform, constant density, and the momentum effect of the shielding gas jet was neglected.

GOVERNING EQUATIONS

The fluid flow behaviour, heat transfer, and evolution of the free surface in the laser beam welding process are described by solving the continuity, Navier-Stokes, energy conservation, and Volume-of-Fluid (VOF) equations. To account for the influence of electromagnetic fields induced by the applied alternating magnetic field, the magnetic induction equation is also incorporated into the three-dimensional computational fluid dynamics model. All governing equations are formulated within a fixed Cartesian coordinate system, as detailed below.

Mass conservation:

$$\nabla \cdot \vec{v} = 0, \tag{1}$$

Where the $\vec{v}$ is the fluid flow velocity.

Navier-Stokes equation:

$$\rho\left(\frac{\partial \vec{v}}{\partial t} + (\vec{v} \cdot \nabla)\vec{v}\right) = -\nabla p + \mu \nabla^2 \vec{v} + \rho \vec{g} + \vec{S}_m, \tag{2}$$

where ρ is the density, t means the time, p is the hydrodynamic pressure, μ is the viscosity, $\vec{g}$ is the gravitational acceleration vector, and $\vec{S}_m$ is the additional momentum source term including the fluid flow in the mushy zone, buoyancy forces, surface tension forces, recoil pressure, vapor-induced stagnation and shear forces, and Lorentz forces.

Energy conservation equation:

$$\rho\left[\frac{\partial h}{\partial t} + (\vec{v} \cdot \nabla)h\right] = \nabla \cdot (k \nabla T) + S_q \tag{3}$$

with the enthalpy h, the thermal conductivity k, and the energy source term S_q accounting for the heat of the laser source, convective and radiative heat transfer, the heat loss of evaporation, heat flux of vapor recondensation, and the heat transfer caused by the vapor induced scattering and absorption effects.

VOF equation:

$$\frac{\partial \phi}{\partial t} + \nabla \cdot (\vec{v}\phi) = 0, \tag{4}$$

where ϕ is the liquid phase volume fraction which is used for the free surface tracking.

Magnetic induction equation:

$$\frac{\partial \vec{b}}{\partial t} + (\vec{v} \cdot \nabla)\vec{b} = \frac{1}{\mu_m \sigma_e} \nabla^2 \vec{b} + \left((\overrightarrow{B_0} + \vec{b}) \cdot \nabla \right) \vec{v} - (\vec{v} \cdot \nabla)\overrightarrow{B_0}, \quad (5)$$

The electromagnetic field within the weld pool was computed using the magnetic induction equation, which is derived from the combination of Ohm's law and Maxwell's equations, as presented in Eq. (5). The resulting secondary magnetic flux density $\vec{b}$ is generated by both the temporal variation of the externally applied magnetic field $\overrightarrow{B_0}$ and the motion of the electrically conductive molten metal. The external magnetic flux density was previously measured under cold conditions [20] and was directly incorporated into the model as an input field.

The induced current density $\vec{j}$ and the corresponding Lorentz force $\overrightarrow{F_L}$ were subsequently calculated according to Eqs. (6) and (7), respectively. The Lorentz force was then introduced as a volumetric source term in the momentum conservation equation to account for electromagnetic effects on the molten metal flow.

$$\vec{j} = \frac{1}{\mu_m} \nabla \times (\overrightarrow{B_0} + \vec{b}), \quad (6)$$

$$\overrightarrow{F_L} = \vec{j} \times (\overrightarrow{B_0} + \vec{b}), \quad (7)$$

where μ_m is the magnetic permeability.

PHYSICAL MODELS

The spatial distribution of laser energy on any horizontal plane within the computational domain is represented by a Gaussian profile, as defined by Eq. (8):

$$q_L = \frac{2}{\pi r_z^2} \cdot \exp(-2\frac{x^2+y^2}{r_z^2}) \cdot (I_0 - \Delta I), \quad (8)$$

Where I_0 is the laser power, ΔI refers to the total amount of laser power attenuation induced by metal vapor plume, r_z denotes the laser beam radius at a given axial position and is defined as:

$$r_z = r_f \left[1 + \left(\frac{z - z_f}{z_r} \right)^2 \right]^{\frac{1}{2}}, \quad (9)$$

To account for multiple reflections and Fresnel absorption at the keyhole walls, a ray-tracing algorithm was employed [21] with a total of 755 sub-rays discretizing the laser energy density according to the Gaussian distribution in Eq. (8). The accuracy of the ray tracing was influenced by the interface resolution of the VOF method and the local mesh size, which limits the smoothness and continuity of the reconstructed keyhole surface. To mitigate this limitation and improve the resolution of ray interactions with the keyhole boundary, the virtual cell refinement technique [22,23] was incorporated, with a minimum cell size of 0.067 mm.

The Fresnel absorption coefficient α was computed using the following equation:

$$\alpha = 1 - \frac{1}{2}\left(\frac{1+(1-\varepsilon cos\varphi)^2}{1+(1+\varepsilon cos\varphi)^2} + \frac{\varepsilon^2 - 2\varepsilon cos\varphi + 2cos^2\varphi}{\varepsilon^2 + 2\varepsilon cos\varphi + 2cos^2\varphi}\right) \quad (10)$$

Where φ is the beam incident angle, ε is an empirically calibrated parameter based on physical properties of the metal and the laser wavelength.

Time-dependent laser attenuation caused by metal vapor plume oscillations was also incorporated into the heat source model. Metallic nanoparticles in the vapor plume condense and remain suspended, contributing to scattering and absorption of the laser beam. While laser beam refraction and inverse Bremsstrahlung absorption are typically negligible for short-wavelength fibre lasers [24], scattering and absorption effects were modelled using Beer's Law [25,26]. The vapor plume length along the laser path was determined experimentally and fitted via Fast Fourier Transform (FFT) analysis. The energy loss from scattering is then redistributed over the top surface of the weld pool following a Gaussian profile, whereas the absorbed energy is delivered through radiation and convection. The momentum transfer from the vapor plume within the keyhole, including stagnation and shear stress components, was also considered [21]. The recoil pressure arising from vaporization was modelled using the approach presented in [20,27].

BOUNDARY CONDITIONS AND NUMERICAL SETUP

A structured hexahedral mesh was generated, featuring a uniform fine mesh with a cell size of 0.2 mm in the central region to accurately capture keyhole dynamics and thermal gradients. In the peripheral regions, a progressively mesh coarsening was applied. The boundary conditions for the air phase domain were defined as pressure outlets with adiabatic thermal boundaries and zero electric current density, representing an electrically insulating and thermally isolated environment. For the aluminium phase, the bottom surface was treated as a no-slip wall, with convective heat loss applied and no electric current allowed through the boundary. To reduce computational costs, the simulation domain was modelled as a representative subsection of the full aluminium sheet. Consequently, the lateral surfaces of the aluminium domain were prescribed as no-slip walls for fluid flow. However, for the thermal and electromagnetic analyses, continuity conditions were imposed across these boundaries [28].

All governing equations were numerically solved using the commercial computational fluid dynamics (CFD) software ANSYS Fluent. A second-order upwind discretization scheme was employed for both the momentum and energy conservation equations to ensure numerical accuracy and stability. The coupling between the pressure and velocity fields was handled using the Pressure-Implicit with Splitting of Operators (PISO) algorithm. The aluminium-gas interface was tracked using the Geo-Reconstruct scheme. The thermophysical properties of the AlMg3 aluminium alloy used in the simulation were reported in a previous study [20].

KEYHOLE RECONSTRUCTION ALGORITHM

In this study, a reconstruction algorithm was developed to reconstruct the time-averaged keyhole geometry and to quantitatively evaluate keyhole stability from a statistical perspective. Given the complexity of the three-dimensional keyhole shape, the concept of an equivalent diameter was introduced to simplify the characterization by reducing the dimensionality of the keyhole geometry.

As shown in Fig. 2, the keyhole domain was firstly discretized along the thickness direction, resulting in a series of horizontal cross-sectional planes. On each plane, the keyhole gas phase region is identified, and its total area is computed. Assuming that the gas-liquid interface on each cross-section can be approximated with a circular shape, the equivalent diameter at a given time step and discrete plane is derived from the gas phase area and then calculate the time-averaged value. To fully reconstruct the keyhole profile, information about the centroid position on each horizontal plane is also required. Assuming that the gas phase density is constant and uniform, the mass centre of the gas phase coincides with its geometric centroid. The calculation equations are shown in Eq. (11) to (14).

$$\sum_j A_{i,j,k} = \frac{\pi {d_{eq}}_{i,k}^{\,2}}{4}, \tag{11}$$

$$\bar{d}_{eq,i} = \frac{1}{t_{k_l} - t_{k_f}} \sum_{k=k_f}^{k_l-1} d_{eq_{i,k}} \cdot (t_{k+1} - t_k), \tag{12}$$

Here, i denotes the the i-th discrete layer, j denotes the index of the cell, k denotes the index of discrete time step, $A_{i,j,k}$ is the area of the air phase in the cell with j index on the i-th layer at k-th time step, $d_{eq_{i,k}}$ means the equivalent diameter on the i-th layer at k-th time step, $\overline{d_{eq_i}}$ denotes the time-averaged equivalent diameter on the i-th layer, t_{k_l} is the physical time corresponding to the k_l time step, t_{k_f} is the physical time corresponding to the k_f time step, k_f means the index of the first time step within the specified time span, k_l means the index of the last time step within the specified time span, t_k is the physical time corresponding to the k-th time step, t_{k+1} is the physical time corresponding to the $(k+1)$-th time step.

$$\bar{x}_i = \frac{1}{t_{k_l} - t_{k_f}} \sum_{k=k_f}^{k_l-1} \left(\frac{\sum_j x_{i,j,k} \cdot A_{i,j,k}}{\sum_j A_{i,j,k}}\right) \cdot (t_{k+1} - t_k) \tag{13}$$

$$\bar{y}_i = \frac{1}{t_{k_l} - t_{k_f}} \sum_{k=k_f}^{k_l-1} \frac{\sum_j y_{i,j,k} \cdot A_{i,j,k}}{\sum_j A_{i,j,k}} \cdot (t_{k+1} - t_k) \tag{14}$$

Here $\bar{x}_i$ and $\bar{y}_i$ means time-averaged centroid x-coordinate and y-coordinate on the i-th layer. $x_{i,j,k}$ and $y_{i,j,k}$ means x and y coordinate value of the cell with j index at the i-th layer and k-th time step. By combining the time-averaged equivalent diameter and centroid position on each cross-sectional plane, a time-averaged 2D keyhole profile is then reconstructed

representing a statistically averaged morphology, providing a more stable and representative description of the keyhole geometry.

Furthermore, the standard deviation of the equivalent diameter over the same time interval provides a quantitative measure of the amplitude of keyhole fluctuations, thereby enabling the assessment of keyhole stability, as shown in Eq. (15).

$$\sigma_i = \sqrt{\frac{\sum_{k=k_f}^{k_l}(d_{eq_{i,k}} - \bar{d}_{eq,i})^2}{k_l - k_f + 1}} \tag{15}$$

Where σ_i is the standard deviation of the keyhole diameter on the i-th layer over a certain time span.

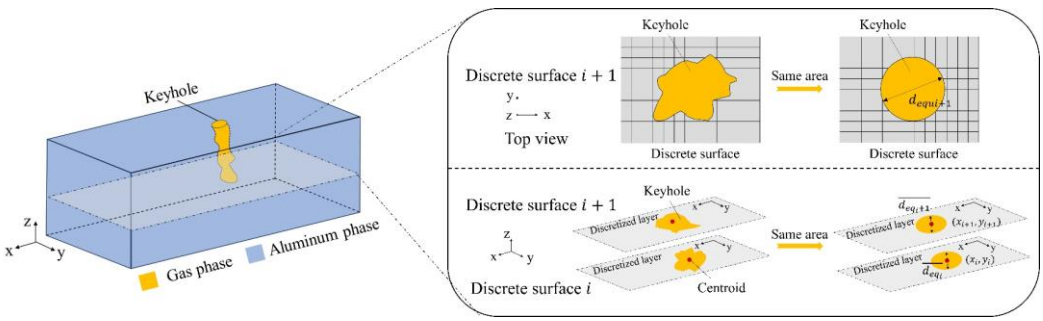

Fig. 2 Schematic of the keyhole reconstruction principle

RESULTS & DISCUSSION

POROSITY RATIO

Fig. 3 illustrates the X-ray inspection results of weld specimens processed with and without the application of magnetic fields. A clear decreasing trend in the porosity ratio is observed with increasing magnetic flux density. Specifically, for the highest applied magnetic flux densities, the porosity ratio decreases to below 1 %.

A noticeable reduction in porosity ratio is observed when a magnetic field is applied as mentioned above, which can be used to infer that keyhole stability is improved. It should be noted that the porosity reduction is not solely controlled by the enhanced keyhole stability. Process porosity during laser beam welding originates from two aspects: (1) the formation of gas bubbles due to a keyhole instability, and (2) the inability of these bubbles to escape the molten pool before being trapped by the advancing solidification front. Oscillating magnetic fields not only influence the keyhole dynamic behaviour but also significantly enhance the

escape of bubbles from the molten pool through an additional electromagnetic expulsive force [20]. To further assess the keyhole stability, this study conducts a statistical analysis based on numerical simulations.

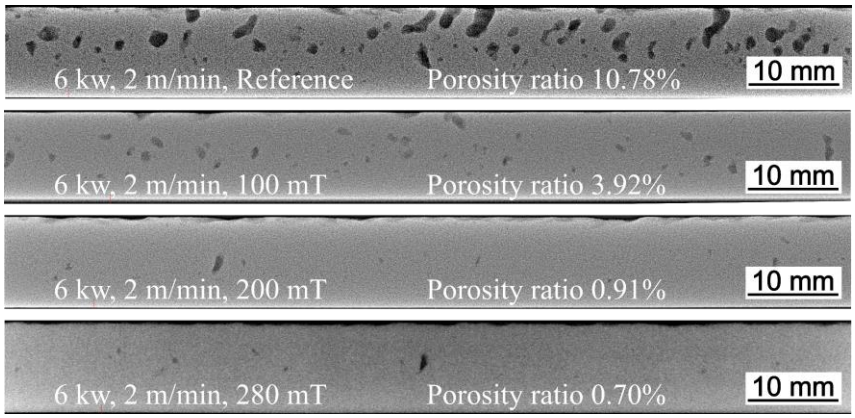

Fig. 3 X-ray results without and with applied magnetic field

MODEL VALIDATION

To assess the accuracy of the developed numerical model, the simulated cross-sectional morphology and dimensions of the weld pool were compared with experimental observations under both the reference condition and a result with a magnetic flux density of 200 mT applied, as shown in Fig. 4. In the comparison, the black dashed lines in the computed cross-sections represent the experimentally determined fusion boundaries. The results indicate that the simulated weld pool profiles exhibit good agreement with the experimental data, confirming the model's reasonable predictive capability. However, our current model does not have the capability to simulate the formation of bubbles and porosity retained in the welded joint. A more detailed validation is presented in [20].

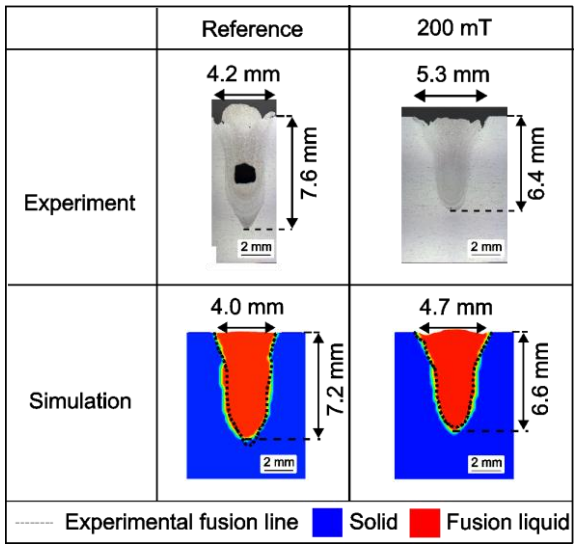

Fig. 4 Comparison of experimental and calculated cross-sections

LIMITATIONS OF ONE-DIMENSIONAL METRICS IN EVALUATING KEYHOLE STABILITY

In prior studies, keyhole stability in LBW has commonly been assessed using one-dimensional measurements of the keyhole depth as a quantitative metric, as discussed above [15]. Following this convention, the present study also evaluates keyhole stability based on the temporal evolution of keyhole depth. Fig. 5 illustrates the time-dependent variations in the keyhole depth. The results reveal that the keyhole depth exhibits significant dynamic fluctuations during welding, making it difficult to assess stability based solely on its temporal variation. Thus, the standard deviation of the keyhole depth is also calculated. A noticeable reduction in the standard deviation of the keyhole depth is observed at 100 mT, suggesting that the keyhole depth fluctuations is suppressed by magnetic field effectively. However, at 200 mT and 280 mT, the standard deviation increases to a level comparable to the reference case, indicating a similar degree of keyhole instability. This observation contradicts the visual evidence from the selected keyhole shapes in Fig. 6, which intuitively show a stabilized keyhole after applying the magnetic field.

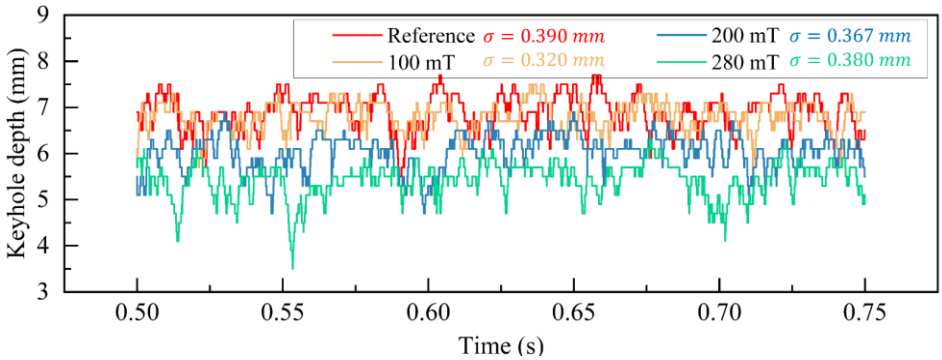

Fig. 5 Temporal keyhole depth and their time-average and standard deviation values

This contradiction shows the limitation of using keyhole depth and keyhole morphologies as metrics for evaluating keyhole stability. The keyhole depth, by its one-dimensional nature, captures only vertical fluctuations and fails to account for instability phenomena that predominantly manifest in the horizontal directions, such as keyhole collapse or protrusions on the keyhole wall. Although these instabilities can indirectly influence the keyhole depth by altering local energy absorption or keyhole wall dynamics, the measured depth variation is merely a secondary effect, not a direct representation of the underlying instability. Moreover, the keyhole morphologies used for comparison can be deliberately selected, rather than being randomly chosen.

In summary, the two conventional approaches employed in this study, namely the keyhole depth fluctuation and the selected transient keyhole morphology, yield inconsistent conclusions regarding keyhole stability, highlighting the inherent limitations of traditional one-dimensional evaluation methods.

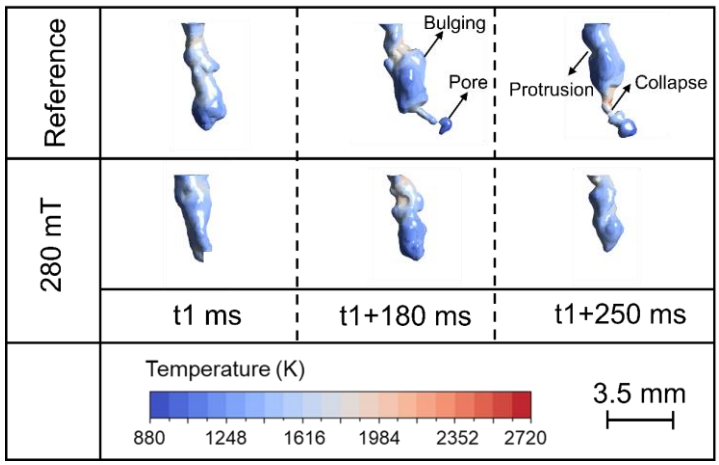

Fig. 6 Transient keyhole shape in reference and MHD case

EFFECT OF MAGNETIC FIELD ON KEYHOLE DIAMETER EVOLUTION

Fig. 7(a) presents the temporal evolution of the equivalent keyhole diameter at a location 1 mm above the keyhole bottom across different magnetic flux densities. The diameter exhibits substantial fluctuations within the range of up to 1.4 mm. Localized temporal variations in keyhole diameter alone are insufficient to provide a comprehensive assessment of overall keyhole stability.

To address this limitation, time-averaged keyhole diameters were analysed across different relative depths (except the elongated keyhole region near the top surface) along the keyhole axis under varying magnetic field conditions, as shown in Fig. 7(b). The results clearly reveal that the time-averaged keyhole diameter decreases with increasing magnetic flux density. This behaviour is consistent with findings from our prior work about LBW of steel [29], which indicate that although the applied magnetic field is oscillatory, the resulting time-averaged Lorentz force acts with a downward direction and increases in magnitude with the magnetic flux density. The enhanced downward Lorentz force compresses the molten metal around the keyhole, leading to a narrower keyhole profile. This effect is pronounced in the mid and lower regions of the keyhole.

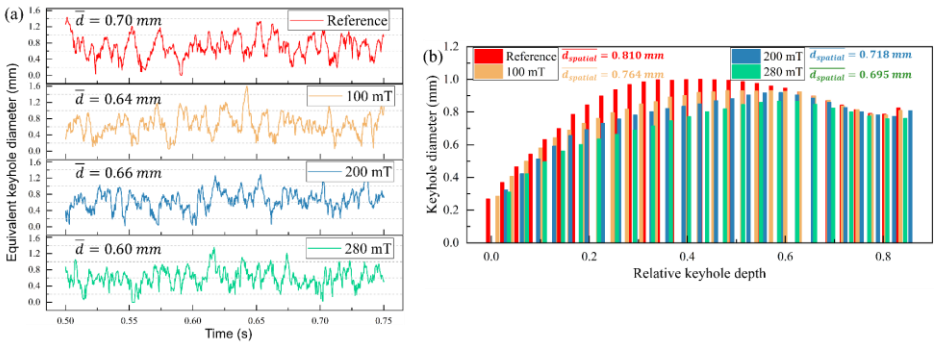

Fig. 7 (A) Equivalent keyhole diameter 1 mm above keyhole bottom and time-average value, (B) Time-average value of the equivalent keyhole diameter and space-average value

KEYHOLE STABILITY EVALUATION

The observed diameter changes provide valuable insights into the complex interaction between electromagnetic forces and melt pool dynamics in laser beam welding. However, they cannot fully indicate changes in the keyhole stability. To quantitatively evaluate keyhole stability, the standard deviation of the keyhole diameter is calculated, which can provide direct statistical evidence of the keyhole fluctuation amplitude and a robust indicator of keyhole stability.

Fig. 8 presents the distribution of the standard deviation of the keyhole diameter along the keyhole depth under different magnetic flux densities. The standard deviation of the keyhole

diameter shows an overall decreasing trend with increasing magnetic flux density. To assess keyhole stability from a global perspective, the space-averaged standard deviation across all discrete layers was calculated for each case. As the magnetic flux density increases, this value decreases progressively from 0.263 mm in the reference case reaching 0.217 mm for the applied highest magnetic flux density of 280 mT. Additionally, the variation of the standard deviation along the keyhole depth is significantly reduced with increasing magnetic flux density.

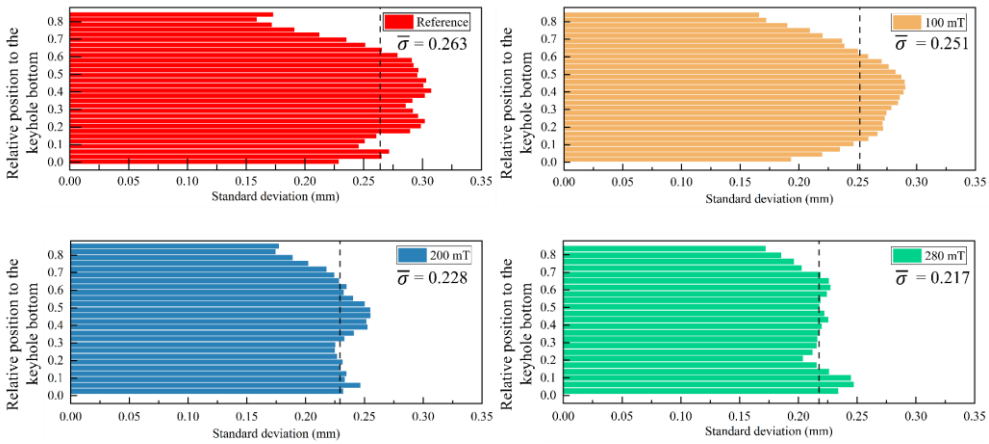

Fig. 8 Distribution of the standard deviation of the equivalent keyhole diameter along the keyhole axis and its space-average for different magnetic flux densities

These findings confirm that the application of external magnetic fields effectively suppress the keyhole fluctuation, resulting in a more stable keyhole. Importantly, this analysis provides statistical evidence from a multi-dimensional perspective by accounting for both spatial and temporal variations in keyhole behaviour. This method overcomes the limitations of traditional one-dimensional metrics and enhances the ability to understand and control dynamic keyhole phenomena under the influence of magnetic fields. It was thus possible to prove that the magnetic forces can stabilise the keyhole, resulting in less keyhole-induced porosity.

KEYHOLE RECONSTRUCTION

The reconstructed time-averaged keyhole profiles using the time-averaged equivalent diameter and centroid position at each discrete keyhole layer are presented in Fig. 9. These profiles provide a statistically robust representations of the keyhole geometry. The laser axis remains consistently aligned closer to the front wall of the keyhole. This is primarily because the initial laser incidence is concentrated on the front wall, resulting in significantly higher energy absorption in that region and initiating the melting of cold base metal ahead of the keyhole, which can be evidenced by the calculation results from Meng [18]. The formation of

the keyhole lags behind the moving laser heat source. Thus, the laser axis appears closer to the front keyhole wall, while the centroid of the keyhole is located behind the laser axis. The reconstructed keyhole profiles can capture the characteristic trailing tail at the bottom of the keyhole. The overall shape of the keyhole is smooth and there is no obvious instability characteristics. The application of external magnetic fields does not fundamentally alter the overall keyhole shape. However, with increasing magnetic flux density, the trailing tail becomes progressively less pronounced, indicating a suppressive effect of the magnetohydrodynamic forces on the rear section of the keyhole. Notably, a significant increase in the curvature of the rear keyhole wall is observed when the magnetic flux density exceeds 200 mT, which may be linked to a redistribution of laser energy deposition, particularly at the rear wall.

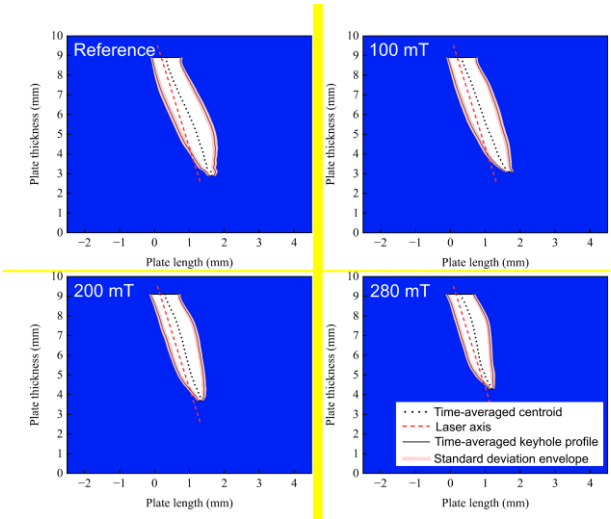

Fig. 9 Reconstructed keyhole shapes under different magnetic flux densities

CONCLUSIONS

A novel keyhole reconstruction approach, combined with a statistical assessment method for evaluating the keyhole stability, was developed based on a transient three-dimensional multi-physics LBW model. The main findings are summarized as follows:

- The limitations of conventional methods for evaluating keyhole stability were demonstrated. The transient keyhole geometry or one-dimensional keyhole depth variations are insufficient and may lead to misleading interpretations due to their inability to capture the full spatial and temporal complexity of the process.
- A time-averaged reconstruction of the keyhole profiles revealed a characteristic smooth geometry without pronounced instability features. The application of external

magnetic fields did not fundamentally alter the overall morphology of the time-averaged keyhole.

- The metric of spatial-average of the standard deviation of keyhole diameter certifies that the magnetic field application can stabilize the keyhole effectively. The degree of stabilization positively correlates with an increasing magnetic flux density.

ACKNOWLEDGEMENTS

This work is funded by the Deutsche Forschungsgemeinschaft (DFG, German Research Foundation)-Project No. 466939224, No. 506270597, and No. 547924277.

References

[1] H. ZHAO, D. R. WHITE, T. DEBROY: 'Current issues and problems in laser welding of automotive aluminium alloys', *International materials reviews*, 44(6), pp. 238-266, 1999.

[2] A. MATSUNAWA, J. D. KIM, N. SETO, M. MIZUTANI, S. KATAYAMA: 'Dynamics of keyhole and molten pool in laser welding', *Journal of laser applications*, 10(6), pp. 247-254, 1998.

[3] H. ZHAO, D. R. WHITE, T. DEBROY: 'Current issues and problems in laser welding of automotive aluminium alloys', *International materials reviews*, 44(6), pp. 238-266, 1999.

[4] S. KATAYAMA (ED.): *Handbook of laser welding technologies*, 2013.

[5] M. CHATURVEDI (ED.): 'Welding and joining of aerospace materials', *Woodhead publishing*, 2020.

[6] J. R. DEEPAK, R. P. ANIRUDH, S. S. SUNDAR: 'Applications of lasers in industries and laser welding: A review', *Materials Today: Proceedings*, 2023.

[7] A. MATSUNAWA, N. SETO, J. D. KIM, M. MIZUTANI, S. KATAYAMA: 'Dynamics of keyhole and molten pool in high-power CO2 laser welding', *High-Power Lasers in Manufacturing*, 3888, pp. 34-45, 2000.

[8] A. F. H. KAPLAN, J. POWELL: 'Spatter in laser welding', *Journal of laser Applications*, 23(3), 2011.

[9] T. FLORIAN, K. SCHRICKER, C. ZENZ, A. OTTO, L. SCHMIDT, C. DIEGEL, H. FRIEDMANN, M. SEIBOLD, P. HELLWIG, F. FRÖHLICH, F. NAGEL, P. KALLAGE, M. BUTTAZZONI, A. RACK, H. REQUARDT, Y. CHEN, J.P. BERGMANN: 'Combining in situ synchrotron X-ray imaging and multiphysics simulation to reveal pore formation dynamics in laser welding of copper', *International Journal of Machine Tools and Manufacture*, 204, 104224, 2025.

[10] F. FETZER, H. HU, P. BERGER, R. WEBER, P. EBERHARD, T. GRAF: 'Fundamental investigations on the spiking mechanism by means of laser beam welding of ice', *Journal of Laser Applications*, 30(1), 2018.

[11] L. WANG, M. YAO, X. GAO, F. KONG, J. TANG, M. J. KIM: 'Keyhole stability and surface quality during novel adjustable-ring mode laser (ARM) welding of aluminum alloy', *Optics & Laser Technology*, 161, 109202, 2023.

[12] J. ZHAO, J. LI, Y. DING, L. BAI, Y. CHENG: 'Quantitative evaluation of keyhole stability during laser welding using optical coherence tomography', *Welding International*, 38(3), pp. 225-238, 2024.

[13] M. MIYAGI, J. WANG: 'Keyhole dynamics and morphology visualized by in-situ X-ray imaging in laser melting of austenitic stainless steel', *Journal of Materials Processing Technology*, 282, 116673, 2020.

[14] D. ZHANG, M. WANG, C. SHU, Y. ZHANG, D. WU, Y. YE: 'Dynamic keyhole behavior and keyhole instability in high power fiber laser welding of stainless steel', *Optics & Laser Technology*, 114, pp. 1-9, 2019.

[15] L. LI, G. PENG, J. WANG, J. GONG, S. MENG: 'Numerical and experimental study on keyhole and melt flow dynamics during laser welding of aluminium alloys under subatmospheric pressures', *International Journal of Heat and Mass Transfer*, 133, pp. 812-826, 2019.

[16] L. HUANG, X. HUA, D. WU, F. LI: 'Numerical study of keyhole instability and porosity formation mechanism in laser welding of aluminum alloy and steel', *Journal of Materials Processing Technology*, 252, pp. 421-431, 2018.

[17] Y. WANG, P. JIANG, S. GENG, B. XU, J. ZHAO: 'Influence of the wrinkle surface structures on the vapor flow and keyhole stability in 20 kW high power laser welding', *International Journal of Heat and Mass Transfer*, 193, 122958, 2022.

[18] X. MENG, S. N. PUTRA, M. BACHMANN, M RETHMEIER: 'A statistical assessment of the laser energy absorption and keyhole stability in high-power laser welding', *Journal of Manufacturing Processes*, 141, pp. 885-896, 2025.

[19] X. MENG, M. BACHMANN, A. ARTINOV, M. RETHMEIER: 'A study of the magnetohydrodynamic effect on keyhole dynamics and defect mitigation in laser beam welding', *Journal of Materials Processing Technology*, 307, 117636, 2022.

[20] F. YANG, X. MENG, S.N. PUTRA, M. BACHMANN, M. RETHMEIER: 'Numerical studies of process porosity suppression by magnetohydrodynamic technology during the laser beam welding of aluminum alloy', *International Journal of Heat and Mass Transfer*, 253, 127525, 2025.

[21] W. I. CHO, S. J. NA, C. THOMY, F. VOLLERTSEN: 'Numerical simulation of molten pool dynamics in high power disk laser welding', *Journal of Materials Processing Technology*, 212(1), pp. 262-275, 2012.

[22] X. MENG, A. ARTINOV, M. BACHMANN, Ö. ÜSTÜNDAĞ, A. GUMENYUK, M. RETHMEIER: 'The detrimental molten pool narrowing phenomenon in wire feed laser beam welding and its suppression by magnetohydrodynamic technique', *International Journal of Heat and Mass Transfer*, 193, 122913, 2022.

[23] S. W. HAN, J. AHN, S. J. NA: 'A study on ray tracing method for CFD simulations of laser keyhole welding: progressive search method', *Welding in the World*, 60, pp. 247-258, 2016.

[24] S. W. HAN, W. I. CHO, L. J. ZHANG, S. J. NA: 'A study on laser keyhole welding in vacuum by computational fluid dynamics simulations with plume effect models', *Journal of Laser Applications*, 33(1), 012042, 2021.

[25] X. MENG, S. N. PUTRA, M. BACHMANN, F. YANG, A. ARTINOV, M. RETHMEIER: 'A fundamental study of physical mechanisms of wineglass-shaped fusion zone profile in laser melting', *Journal of Materials Processing Technology*, 324, 118265, 2024.

[26] F. YANG, X. MENG, S. N. PUTRA, A. ARTINOV, M. BACHMANN, M. RETHMEIER: 'Numerical analysis of the effect of an oscillating metal vapor plume on the keyhole and molten pool behavior during deep penetration laser beam welding', *Journal of Laser Applications*, 35(4), 042041, 2023.

[27] S. PANG, X. CHEN, J. ZHOU, X. SHAO, C. WANG: '3D transient multiphase model for keyhole, vapor plume, and weld pool dynamics in laser welding including the ambient pressure effect', *Optics and Lasers in Engineering*, 74, pp. 47-58, 2015.

[28] X. MENG, G. QIN, R. ZONG: 'Thermal behavior and fluid flow during humping formation in high-speed full penetration gas tungsten arc welding', *International Journal of Thermal Sciences*, 134, pp. 380-391, 2018.

[29] F. YANG, X. MENG, S. N. PUTRA, M. BACHMANN, M. RETHMEIER: 'Assessment of keyhole stability in laser beam welding with external magnetic field using numerical simulation', *Journal of Laser Applications*, 36(4), 042038, 2024.